PHYSICAL REVIEW B **89**, 125313 (2014)

Magnetic control of Coulomb scattering and terahertz transitions among excitons

J. Bhattacharyya,[1] S. Zybell,[1,2] F. Eßer,[1,2] M. Helm,[1,2] H. Schneider,[1,*] L. Schneebeli,[3] C. N. Böttge,[3] B. Breddermann,[3]
M. Kira,[3] S. W. Koch,[3] A. M. Andrews,[4] and G. Strasser[4]
[1] *Helmholtz-Zentrum Dresden-Rossendorf, Post Office Box 510119, 01314 Dresden, Germany*
[2] *Technische Universität Dresden, 01062 Dresden, Germany*
[3] *Department of Physics and Material Sciences Center, Philipps-Universität Marburg, Renthof 5, 35032 Marburg, Germany*
[4] *Institute of Solid State Electronics, Technische Universität Vienna, Floragasse 7, 1040 Vienna, Austria*

(Received 23 September 2013; revised manuscript received 11 March 2014; published 31 March 2014)

Time-resolved terahertz quenching studies of the magnetoexcitonic photoluminescence from GaAs/AlGaAs quantum wells are performed. A microscopic theory is developed to analyze the experiments. Detailed experiment-theory comparisons reveal a remarkable magnetic-field controllability of the Coulomb and terahertz interactions in the excitonic system.

DOI: 10.1103/PhysRevB.89.125313 PACS number(s): 78.67.De, 71.35.−y, 75.75.−c, 78.55.Cr

I. INTRODUCTION

The exciton is a Coulomb-bound electron-hole pair that is similar to a hydrogen atom [1]. Even though excitons in semiconductors only have binding energies in the terahertz ($1\,THz \mathrel{\widehat{=}} 4.1$ meV) range, they strongly influence interband optical properties [2–4], which can critically alter the characteristics of optoelectronic and photonic devices [5–7]. Therefore, nanotechnology applications may be significantly expanded if one is able to systematically control excitons and their fundamental interactions. Exciton-exciton interactions can also steer many novel phenomena such as exciton condensation [8] as well as efficient quantum-state transfer [9,10]. Therefore, precise new schemes to control exciton-exciton interaction can provide new possibilities to a wide range of investigations.

A magnetic field can considerably modify both electronic and excitonic properties. For example, free electrons become bound to Landau levels that can be detected as the quantum Hall effect [11,12]. Furthermore, a magnetic field enhances the binding of excitons; the resulting magnetoexcitons have a reduced Bohr radius and scattering time. This feature has been utilized, e.g., to reach the regime of super-radiance [13] with the help of a magnetic field.

Excitons themselves can directly be accessed by terahertz (THz) spectroscopy, revealing the exciton-formation dynamics as well as internal exciton transitions [14–16], excitonic Rabi oscillations [17], and high-order sideband generation [18]. In addition, a resonant microcavity transforms the polaritonic $1s$ and the optically dark $2p$ states into a Λ system [19]. Furthermore, the Coulomb interaction effectively couples excited exciton states, leading to transitions that are dipole forbidden in a noninteracting system [20].

We demonstrate in this work that certain combinations of THz and magnetic fields (B fields) can be used to precisely control exciton-exciton interactions as well as exciton ionization. We use a B field to generate magnetoexcitons [21,22] and a THz field to provide transitions in between them. These magnetoexcitons have modified energies and wave functions compared to excitons and, in analogy to the Zeeman splitting, the degeneracy of excitons with different magnetic quantum numbers m is lifted [21,22].

Figure 1 visualizes the interplay of B field, Coulomb scattering, and THz-induced transitions among the ground state ($1s$) and two excited states ($2p$, $2s$). As shown in [20], the Coulomb scattering can cooperate with THz transitions to produce an efficient transfer between $2p$ and $2s$ excitons when the THz field is resonant with the $1s$-to-$2p$ transition. More specifically, the Coulomb scattering displaces the relative momentum of 2s excitons. The rate of such scattering is determined by the spatial overlap between a stationary $2p$ and a displaced $2s$ exciton wave function. We will show that the $2p$-to-$2s$ scattering rate can be significantly modified in the presence of a magnetic field.

Figure 1 illustrates stationary $\lambda = (1s,\mathbf{0})$ (bottom) and $\lambda = (2p,\mathbf{0})$ (middle) as well as displaced $\lambda = (2s,\mathbf{q})$ (top) exciton wave functions $\varphi_\lambda(\mathbf{r})$ without magnetic field (left) and with (right) a $B = 2.1\,T$ field. The Coulomb scattering induces a momentum displacement $\hbar\mathbf{q}$ to this $2s$ wave function, i.e., $\varphi_{2s,\mathbf{q}}(\mathbf{r}) = \varphi_{2s,\mathbf{0}}(\mathbf{r})\,e^{i\mathbf{q}\cdot\mathbf{r}}$. The spiral shape of the stationary $2p$ wave function originates from density-dependent terms within the generalized Wannier equation [1] that defines the exciton wave function, and the "interference pattern" in the $2s$ scattering states stems from its $e^{i\mathbf{q}\cdot\mathbf{r}}$ part. We have moved the $1s$, $2p$, and $2s$ wave functions in the y direction to enhance the visibility. For vanishing B field, $\varphi_{2s,\mathbf{q}}$ and $\varphi_{2p,\mathbf{0}}$ have a large overlap integral since the plane-wave part removes their orthogonality. However, already at $B = 2.1\,T$, the magnetic-field effects dominate over Coulomb effects, as seen from the weakened interference pattern in $\varphi_{2s,\mathbf{q}}$ which is strongly contracted as well. Hence, the magnetic field tends to make $2p$ and displaced $2s$ states orthogonal, yielding a strongly reduced Coulombic scattering strength. At the same time, the $1s$-to-$2p$ THz-transition strength (gray arrow) increases for elevated B fields due to the contraction of the exciton wave functions. Hence, we should be able to gradually switch off the $2p$-to-$2s$ scattering by increasing the B field.

II. EXPERIMENT

We excite the $1s$-to-$2p$ transition of quantum well (QW) excitons by a free-electron laser, emitting wavelength-tunable (3–200 μm), picosecond (ps)-long THz pulses. These excitons

---

[*] corresponding author: h.schneider@hzdr.de

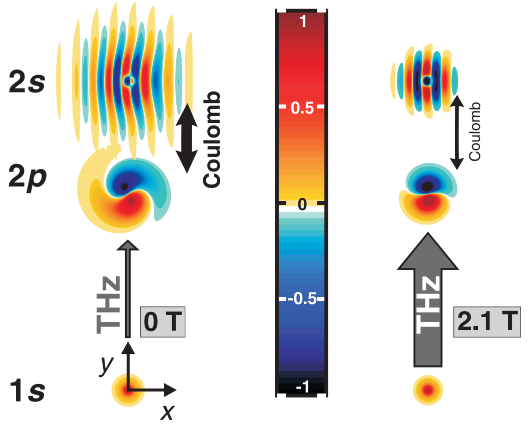

FIG. 1. (Color online) Influence of a magnetic field on THz and Coulomb interactions. Computed exciton wave functions are shown. Horizontal and vertical directions represent spatial coordinates. Note that the $2p$ and $2s$ energies (not shown) are B dependent and presented in Fig. 4(a); for details, see text.

are produced by near-infrared (NIR) interband excitation at a fluence of 0.15 μJ/cm^2 using a Ti:sapphire laser emitting 4-ps pulses at 1.627 eV. We use a high-quality multiple QW structure grown by molecular-beam epitaxy on a semi-insulating GaAs substrate. The sample comprises 60 GaAs QWs of 8.2-nm width separated by 19.6-nm-wide AlGaAs barriers. The heavy-hole $1s$ excitonic state, the lowest energy level in the QWs, is at 1.566 eV with a linewidth of 3 meV, as inferred from absorption measurements at 10 K [17], while the quasidegenerate $2s$ and $2p$ excitonic states are located at 1.575 eV. The light-hole excitonic $1s$ energy is still higher, at 1.583 eV [17]. We focus both lasers onto the sample and detect the photoluminescence (PL) by a synchroscan streak camera [23]. Allowing about 600 ps prior to the THz pulse for exciton formation and cooling [24,25], practically a pure occupation of the $1s$ excitonic state is prepared.

Figure 2 shows the measured PL spectra with THz field (PL$_{\rm on}$, solid) and without THz field (PL$_{\rm off}$, dashed) for $B = 0.0\,T$ [Fig. 2(a)] and $B = 2.1\,T$ [Fig. 2(b)]. The $1s$ and $2s$ emission peaks are labeled and the dashed vertical lines mark the integration area. We have normalized the PL such that the energy-integrated THz-off case produces unity at the $1s$-emission resonance. The THz energy is fixed to 8.7 meV and is resonant with the $1s$-to-$2p$ transition energy without magnetic field. The spectral region above 5 meV has been rescaled by a factor of 60 to enhance the visibility of the $2s$ peak, as indicated by the shaded area.

In Fig. 2(a), we observe that an appreciable amount of $1s$ PL is quenched due to the resonant THz excitation; compare PL$_{\rm on}$ with PL$_{\rm off}$. At the same time, the THz field induces a well-resolved excess $2s$-PL peak. When we increase the B field to 2.1 T [Fig. 2(b)], PL$_{\rm on}$ around the $1s$-emission energy is only weakly modified compared to the B-field-free case. In other words, the $1s$-quenching level is only weakly modified through the B field. However, PL$_{\rm on}$ and PL$_{\rm off}$ around the $2s$-emission energy are almost identical for $B = 2.1\,T$. Hence, the B field almost completely suppresses the generation of $2s$ excess PL. Moreover, the PL spectra nicely show the actual $1s$ and $2s$ emission peaks when a THz field is present or switched off. In the following, the differential PL spectrum is used for the analysis because it presents a convenient tool to isolate the THz-induced changes directly.

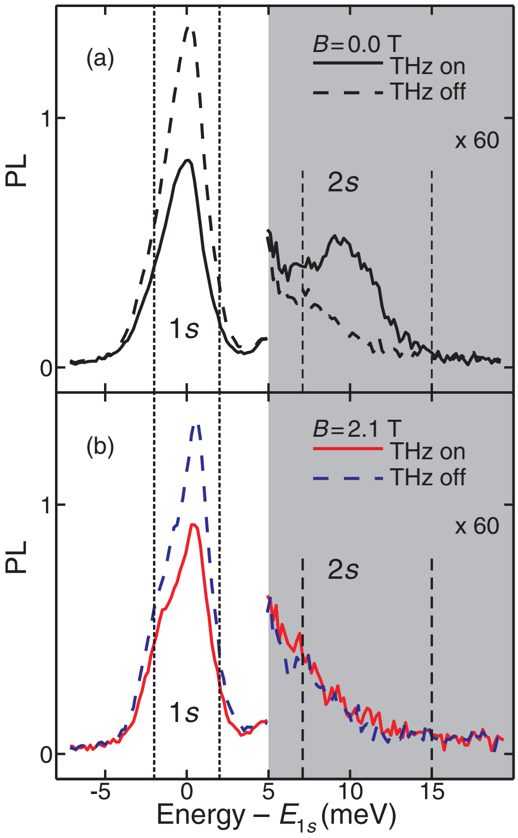

FIG. 2. (Color online) Measured PL spectra for (a) $B = 0.0\,T$ and (b) $B = 2.1\,T$ with (solid) and without (dashed) THz excitation. The THz energy is set to 8.7 meV and is resonant with the $1s$-to-$2p$ transition energy without magnetic field.

Figure 3 shows the effect of THz and magnetic fields on the measured differential PL spectrum denoted as $\Delta\mathrm{PL} = \mathrm{PL}_{\rm on} - \mathrm{PL}_{\rm off}$ that is the difference of the PL with THz (PL$_{\rm on}$) and without THz (PL$_{\rm off}$) field. The THz energy is set to 8.7 meV and is resonant with the $1s$-to-$2p$ transition energy without magnetic field. The black (red) line shows ΔPL for $B = 0\,T$ ($B = 2.1\,T$), shortly (16 ps) after the THz-pulse center coincides with the QW. Above 5 meV (shaded area), the spectra have been rescaled by a factor of 30 to enhance

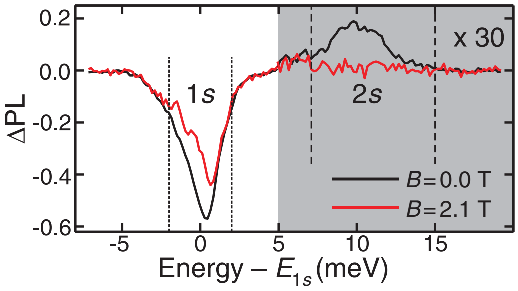

FIG. 3. (Color online) Measured differential PL spectra.

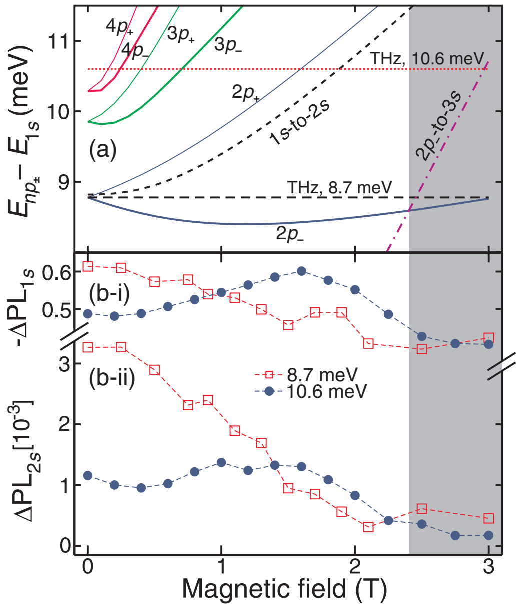

FIG. 4. (Color online) Magnetic-field control of intraexciton transitions. (a) Computed transition energy from $1s$ to $np_\pm$ exciton states as a function of B. (b) Experimental data of (b-i) $1s$ quench and (b-ii) $2s$ excess PL as a function of B. Dashed lines are a guide to the eye. The shaded area indicates the new two-photon resonance.

the visibility of the $2s$ peak. We observe that PL_{1s} is quenched without B field to a level that decreases only weakly as B is increased to $2.1\,T$. Without B field, we notice a well-pronounced $2s$ enhancement at $0\,T$, i.e., $\Delta PL_{2s} > 0$, which vanishes completely for $B = 2.1\,T$. To analyze $1s$- and $2s$-PL effects directly, we spectrally integrate ΔPL over the regions indicated by the dashed vertical lines in Fig. 3. This procedure isolates the THz-induced changes in the $1s$ (ΔPL_{1s}) and $2s$ (ΔPL_{2s}) emission.

Figure 4(a) shows the calculated dipole-allowed transition energies between $1s$ and p-like states as a function of B field, constructing a fan chart of magnetoexcitons [26,27]. The p-like states are classified by the main quantum number $n \geqslant 2$, angular momentum quantum number $l = 1$, and magnetic quantum number $m = -1$ ($m = +1$) for np_- (np_+) states. The $1s$-to-np_- ($1s$-to-np_+) exciton transition energies are shown as thick solid (thin solid) lines. The $1s$-to-$2s$ ($2p_-$-to-$3s$) energy difference is also presented as a dashed (dashed-dotted) curve. We expect that scattering from $2p_-$ to $2s$ is weaker compared to $2p_+$ to $2s$ because the $2s$ state (dashed curve) is energetically closer to the $2p_+$ state. In agreement with [28–30], the p_- branch first redshifts before it is eventually blueshifted, while the $2p_+$ branch always shows a monotonically increasing blueshift [28–30].

Experimentally, we change the magnetic-field strength B for a fixed THz energy $\hbar\omega_{\text{THz}} = 8.7$ (dashed horizontal line) or 10.6 meV (dotted horizontal line) and record ΔPL_λ at the $\lambda = 1s$ and $2s$ resonances. The $\hbar\omega_{\text{THz}} = 8.7$ meV excitation energy is resonant with the $1s$-to-$2p$ transition at $0\,T$ while $\hbar\omega_{\text{THz}} = 10.6$ meV is resonant with the $1s$-to-$2p_+$ transition at $1.6\,T$. The $\hbar\omega_{\text{THz}} = 8.7$ meV excitation energy is mostly resonant with the $2p_-$ branch for elevated B because the $2p_+$ branch quickly becomes nonresonant for increased B. For $\hbar\omega_{\text{THz}} = 10.6$ meV, the $2p_+$ state becomes resonant with THz transitions at $B = 1.6\,T$.

Figure 4(b-i) shows the measured maximum $-\Delta PL_{1s}$ as a function of B for $\hbar\omega_{\text{THz}} = 8.7$ meV (squares) and $\hbar\omega_{\text{THz}} = 10.6$ meV (circles). The corresponding $\Delta PL_{2s}(B)$ data are shown in Fig. 4(b-ii). For $\hbar\omega_{\text{THz}} = 8.7$ meV and $B = 0\,T$, the THz field transfers $1s$ excitons identically to both $2p_+$ and $2p_-$ excitons because they are degenerate. This generates a large quench observed in ΔPL_{1s}. For higher B values, the $2p_+$ state becomes nonresonant very quickly such that only $2p_-$ is near-resonant with the THz field. Hence, the $1s$ quench results from the THz coupling between $1s$ and $2p_-$ states for elevated B, while the $2p_+$ becomes uncoupled. Consequently, $-\Delta PL_{1s}$ drops monotonically by roughly 40% until $2\,T$. For the same conditions, ΔPL_{2s} drops drastically by a factor of 7. In particular, the large changes in ΔPL_{2s} compared to moderate changes in ΔPL_{1s} demonstrate directly that the B field efficiently controls the Coulomb scattering that directly influences only the ΔPL_{2s} part. As predicted by Fig. 4(a), the $2p_-$ branch becomes resonant again. Also this is observed in the 2–3-T range where $-\Delta PL_{1s}$ starts to increase by 3%.

In addition, a feature emerges to ΔPL_{2s} starting at $B = 2\,T$ for $\hbar\omega_{\text{THz}} = 8.7$ meV: The monotonically decaying trend does not continue, but data points indicate the presence of a resonance above $B = 2.5\,T$, as highlighted by the shaded area. Even though the resonance is small, the experiment resolves it clearly above the otherwise monotonically decaying trend. On the basis of our microscopic theoretical analysis explained in Sec. III, we assign this resonance to a resonant two-photon transition from $1s$ to $3s$ [see Fig. 5(c), dashed line] via the $2p_-$ state and subsequent relaxation toward $2s$. Similar internal

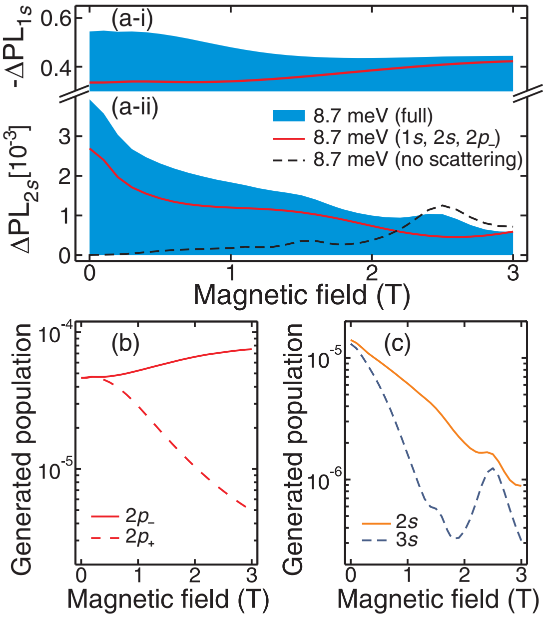

FIG. 5. (Color online) Computed magnetic-field control of intraexciton transitions. Computed (a-i) $1s$ quench and (a-ii) $2s$ excess PL as a function of B. (b, c) Generated (b) p-like and (c) s-like exciton populations as a function of B, based on the full calculation. In all frames, the THz central energy is 8.7 meV and resonant with the $1s$-to-$2p$ transition at $0\,T$.

two-photon transitions have been observed in [15] between $1s$, $2p$, and $2s$ states for high B fields up to 12 T. To distinguish the $2p_-$-to-$3s$ resonance from the scattering-induced $2p$-to-$2s$ transfer, one must have a significantly weakened Coulomb-scattering induced $\Delta\mathrm{PL}_{2s}$, which is the case above $B = 2\,T$. This effect is consequently seen in the tails of $\Delta\mathrm{PL}_{2s}$. Hence, the B field helps to reveal multiphoton THz transitions due to the reduced Coulomb-scattering strength.

For the initially ($0\,T$) detuned $\hbar\omega_{\mathrm{THz}} = 10.6\,\mathrm{meV}$ excitation (circles), we observe a resonance both in $-\Delta\mathrm{PL}_{1s}$ and $\Delta\mathrm{PL}_{2s}$ at around $1.6\,T$. Figure 4(a) shows that $1s$-to-$2p_+$ transition becomes then resonant while neither $2p_+$ or $2p_-$ becomes resonant as B is detuned away from $B = 1.6\,T$. This explains that the detuned case produces a $\Delta\mathrm{PL}_{1s}$ quenching resonance around $B = 1.6\,T$. However, the quench behavior for $\hbar\omega_{\mathrm{THz}} = 10.6\,\mathrm{meV}$ is asymmetric, yielding more quenching (50%) at $B = 0\,T$ compared to $B = 3\,T$ (40%). This is consistent with Fig. 4(a) because there are more nearby final states at $0\,T$ than at $3\,T$. Also $\Delta\mathrm{PL}_{2s}$ shows a maximum at $1.6\,T$, which follows as the $2p_+$ population is transferred into $2s$ population via the Coulomb scattering. As for the $\hbar\omega_{\mathrm{THz}} = 8.7\,\mathrm{meV}$ excitation, the Coulomb scattering is reduced for elevated B such that $\Delta\mathrm{PL}_{2s}(B)$ decreases for $B > 1.6\,T$. At the same time, the maximum of $\Delta\mathrm{PL}_{2s}(B)$ remains smaller compared with the $\hbar\omega_{\mathrm{THz}} = 8.7\,\mathrm{meV}$ case because the Coulomb scattering is already significantly reduced at the peaking $B = 1.6\,T$ field. Hence, many-body effects can be turned on or off individually by choosing the correct THz frequency and B field. This leads to intriguing and unexpected control possibilities.

III. THEORY AND DISCUSSION

Our theory [1,31] starts from the standard many-body Hamiltonian that includes the electronic band structure, the Coulomb interactions among the charge carriers, as well as the light-field and THz interactions. To account for the B field, we use the Hamiltonian [32]:

$$\hat{H}_B = \frac{\hat{\mathbf{p}}^2}{2\mu} + \frac{\hat{\mathbf{P}}^2}{2M} - V(\mathbf{r}) + \frac{\mu}{2}\bar{\boldsymbol{\omega}}_\mu^2\mathbf{r}_\parallel^2 + \frac{|\bar{\boldsymbol{\omega}}_{\mathrm{e}}| - |\bar{\boldsymbol{\omega}}_{\mathrm{h}}|}{2}\hat{L}_z + \bar{\boldsymbol{\omega}}_M\cdot(\mathbf{r}\times\hat{\mathbf{P}}),$$

which leads to the magnetoexcitons [27] when solving the generalized Wannier equation. Here, the relative (center-of-mass) coordinate is denoted as $\mathbf{r}$ ($\mathbf{R}$) with momentum $\hat{\mathbf{p}}$ ($\hat{\mathbf{P}}$) and QW in-plane component $\mathbf{r}_\parallel$. The reduced mass (μ) and total mass (M) enter together with the Coulomb interaction $V(\mathbf{r})$; effective cyclotron frequencies $\bar{\boldsymbol{\omega}}_j$, where e and h denote electron and hole, respectively; and angular momentum operator $\hat{L}_z$. We solve the exciton dynamics [20,32] in the presence of THz and B fields for all relevant bright and dark exciton states and compute the resulting PL via the Elliott formula.

Figure 5 shows the computed $-\Delta\mathrm{PL}_{1s}$ [Fig. 5(a-i)] and $\Delta\mathrm{PL}_{2s}$ [Fig. 5(a-ii)] as a function of B for the $\hbar\omega_{\mathrm{THz}} = 8.7\,\mathrm{meV}$ excitation. The full calculation (shaded area) is compared with reduced calculations having only transitions between the $1s$, $2s$, and $2p_-$ states (dark solid) or vanishing Coulomb scattering (dashed line). The results of the full calculations (shaded area) agree well with the $\hbar\omega_{\mathrm{THz}} = 8.7\,\mathrm{meV}$ excitation [Fig. 4(b) vs Fig. 5(a)].

Due to this quantitative agreement, we can identify the effect of the individual interaction processes on the measured B-field control. For example, excluding the transitions to $2p_+$ [Fig. 5(a-i), dark line] reduces the $1s$ quench by approximately a factor of $\sqrt{2}$ at $B = 0\,T$ because only *one* $2p$ state remains available for transitions. For high B, however, the p_+-excluded calculation approaches the full calculation (shaded area). However, the $2p_+$ and $3s$ states do not affect the $\Delta\mathrm{PL}_{2s}$ significantly, except close to the peak at $B = 2.5\,T$. We find that this resonance follows from a resonant $2p_-$-to-$3s$ transition that is included only to the full (shaded) and vanishing-scattering (dashed line) computations; see also the $2p_-$-to-$3s$ energy difference [Fig. 4(a)] that becomes resonant with the THz field at $B = 2.5\,T$. These switch-off analyses confirm conclusively that the experimental $\Delta\mathrm{PL}_{2s}$ peak in Fig. 4(b-ii) indeed originates from the eventual transition to the $3s$ state.

We have also computed the peak differences in the THz-generated exciton population ΔN_λ. Figure 5(b) analyzes $\Delta N_{2p_\pm}$ and Fig. 5(c) shows ΔN_{2s} and ΔN_{3s} as functions of B. We observe that the THz field dominantly excites a $2p_-$ population that increases slightly for elevated B. Furthermore, the $2p_\pm$ populations are the same only at $0\,T$. At the same time, the $2s$ population decreases by more than one order of magnitude because the increased B field decreases the Coulomb scattering. The THz-induced ΔN_{3s} displays a clear resonance at $2.5\,T$, providing independent evidence that the experimental $\Delta\mathrm{PL}_{2s}$ resonance stems from the $1s$-$2p_-$-$3s$ transition.

Figure 6 presents a similar analysis as in Fig. 5(a), but now for the initially detuned THz excitation $\hbar\omega_{\mathrm{THz}} = 10.6\,\mathrm{meV}$. The computed $-\Delta\mathrm{PL}_{1s}$ [(a)] and $\Delta\mathrm{PL}_{2s}$ [(b)] are shown based on the full (shaded area) and reduced calculations with a four-level model containing only $1s$, $2s$, and $2p_\pm$ states (dark solid line) and without scattering (dashed line). Also for this detuning, the full computation reproduces the experimental $-\Delta\mathrm{PL}_{1s}$ and $\Delta\mathrm{PL}_{2s}$ presented in Fig. 4(b) (circles).

The switch-off analysis of Fig. 6 shows that the four-level calculation (dark solid line) deviates from the full $-\Delta\mathrm{PL}_{1s}$ (shaded area) for B below $1\,T$. This follows because the higher exciton branches ($n\ p_\pm$ for $n \geqslant 3$) are near-resonant with the $\hbar\omega_{\mathrm{THz}} = 10.6\,\mathrm{meV}$ excitation for low-enough B; see Fig. 4(a).

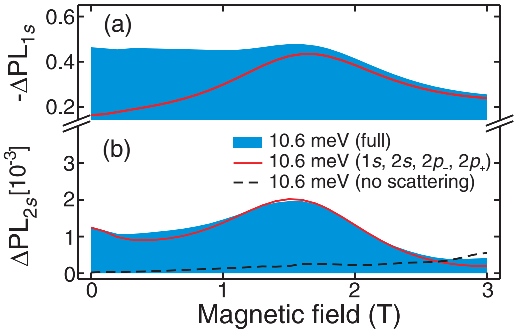

FIG. 6. (Color online) Computed magnetic-field control for $\hbar\omega_{\mathrm{THz}} = 10.6\,\mathrm{meV}$. Computed (a) $1s$ quench and (b) $2s$ excess PL as a function of B.

Consequently, we observe enhanced quenching at $B = 0\,T$ compared with $B = 3\,T$ [Fig. 6(a), shaded], yielding a similar asymmetric behavior as in the experiment [Fig. 4(b-i), circles]. At the same time, $\Delta\mathrm{PL}_{2s}$ is modified only slightly because it originates mainly from the Coulomb scattering between $2p_\pm$ and $2s$ already included in the four-level analysis. For B fields beyond $1.6\,T$, the full and four-level calculations are similar because only the four included states remain near-resonant such that the B field renders the system four-level like. By omitting the Coulomb scattering, the computation almost completely suppresses $\Delta\mathrm{PL}_{2s}$ (dashed line), similar to Fig. 5(a-ii), while $-\Delta\mathrm{PL}_{1s}$ is almost unchanged (not shown). Hence, the diffusive Coulomb scattering is essential for all excitation conditions to correctly describe the scattering-induced $2p$-to-$2s$ population transfer.

IV. CONCLUSIONS

In summary, our experiment identifies combinations of THz and magnetic fields that considerably change the exciton-interaction effects. At intermediate magnetic fields, exciton ionization can be almost eliminated while exciton-exciton scattering remains important. At large magnetic fields, also exciton-exciton scattering can be significantly reduced, yielding almost two-level-system-like THz transitions among $1s$ and $2p$ excitons. At the same time, our many-body theory confirms that competing processes such as THz-transition probability, many-body interactions, and THz ionization can indeed be turned on or off one by one by choosing the correct THz frequency and magnetic field. The realized THz and B-field control can potentially be extended to steer a more general class of many-body interactions.

ACKNOWLEDGMENTS

The Dresden group thanks P. Michel, W. Seidel, and the FELBE team for their dedicated support. The work in Dresden (JB) was partially supported by the Deutsche Forschungsgemeinschaft (DFG) project SCHN 1127/2-1. The Marburg group is thankful for financial support by the DFG projects KI 917/2-1 and RTG 1782.

---

[1] M. Kira and S. W. Koch, *Semiconductor Quantum Optics*, 1st ed. (Cambridge University, Cambridge, 2011).

[2] D. A. B. Miller, D. S. Chemla, T. C. Damen, A. C. Gossard, W. Wiegmann, T. H. Wood, and C. A. Burrus, Phys. Rev. Lett. **53**, 2173 (1984).

[3] S. Schmitt-Rink, D. S. Chemla, and D. A. B. Miller, Adv. Phys. **38**, 89 (1989).

[4] S. W. Koch, M. Kira, G. Khitrova, and H. M. Gibbs, Nature Mater. **5**, 523 (2006).

[5] R. J. Warburton, C. Schäflein, D. Haft, F. Bickel, A. Lorke, K. Karrai, J. M. Garcia, W. Schoenfeld, and P. M. Petroff, Nature (London) **405**, 926 (2000).

[6] F. N. Xia, M. Steiner, Y. M. Lin, and P. Avouris, Nature Nanotech. **3**, 609 (2008).

[7] N. M. Gabor, Z. H. Zhong, K. Bosnick, J. Park, and P. L. McEuen, Science **325**, 1367 (2009).

[8] H. Deng, H. Haug, and Y. Yamamoto, Rev. Mod. Phys. **82**, 1489 (2010).

[9] T. A. Palomaki, J. W. Harlow, J. D. Teufel, R. W. Simmonds, and K. W. Lehnert, Nature (London) **495**, 210 (2013).

[10] T. A. Palomaki, J. D. Teufel, R. W. Simmonds, and K. W. Lehnert, Science **342**, 710 (2013).

[11] M. Kohl, D. Heitmann, P. Grambow, and K. Ploog, Phys. Rev. Lett. **63**, 2124 (1989).

[12] I. Bloch, J. Dalibard, and W. Zwerger, Rev. Mod. Phys. **80**, 885 (2008).

[13] G. T. Noe, II, J. H. Kim, J. Lee, Y. R. Wang, A. K. Wójcik, S. A. McGill, D. H. Reitze, A. A. Belyanin, and J. Kono, Nature Phys. **8**, 219 (2012).

[14] M. S. Salib, H. A. Nickel, G. S. Herold, A. Petrou, B. D. McCombe, R. Chen, K. K. Bajaj, and W. Schaff, Phys. Rev. Lett. **77**, 1135 (1996).

[15] J. Kono, M. Y. Su, T. Inoshita, T. Noda, M. S. Sherwin, S. J. Allen, and H. Sakaki, Phys. Rev. Lett. **79**, 1758 (1997).

[16] R. A. Kaindl, M. A. Carnahan, D. Hägele, R. Lövenich, and D. S. Chemla, Nature (London) **423**, 734 (2003).

[17] M. Wagner, H. Schneider, D. Stehr, S. Winnerl, A. M. Andrews, S. Schartner, G. Strasser, and M. Helm, Phys. Rev. Lett. **105**, 167401 (2010).

[18] B. Zaks, R. B. Liu, and M. S. Sherwin, Nature (London) **483**, 580 (2012).

[19] J. L. Tomaino, A. D. Jameson, Y. S. Lee, G. Khitrova, H. M. Gibbs, A. C. Klettke, M. Kira, and S. W. Koch, Phys. Rev. Lett. **108**, 267402 (2012).

[20] W. D. Rice *et al.*, Phys. Rev. Lett. **110**, 137404 (2013).

[21] J. B. Stark, W. H. Knox, D. S. Chemla, W. Schafer, S. Schmitt-Rink, and C. Stafford, Phys. Rev. Lett. **65**, 3033 (1990).

[22] H. Haug and S. W. Koch, *Quantum Theory of the Optical and Electronic Properties of Semiconductors*, 5th ed. (World Scientific, Singapore, 2009).

[23] J. Bhattacharyya, M. Wagner, S. Zybell, S. Winnerl, D. Stehr, M. Helm, and H. Schneider, Rev. Sci. Instrum. **82**, 103107 (2011).

[24] S. Chatterjee, C. Ell, S. Mosor, G. Khitrova, H. M. Gibbs, W. Hoyer, M. Kira, S. W. Koch, J. P. Prineas, and H. Stolz, Phys. Rev. Lett. **92**, 067402 (2004).

[25] S. Zybell, H. Schneider, S. Winnerl, M. Wagner, K. Kohler, and M. Helm, Appl. Phys. Lett. **99**, 041103 (2011).

[26] J. C. Maan, *Physics and Applications of Quantum Wells and Superlattices*, NATO ASI Series, Vol. 170, edited by E. E. Mendez and K. von Klitzing (Plenum, New York, 1987), pp. 347–375.

[27] S. Schmitt-Rink, J. B. Stark, W. H. Knox, D. S. Chemla, and W. Schäfer, Appl. Phys. A **53**, 491 (1991).

[28] H. A. Nickel, G. Kioseoglou, T. Yeo, H. D. Cheong, A. Petrou, B. D. McCombe, D. Broido, K. K. Bajaj, and R. A. Lewis, Phys. Rev. B **62**, 2773 (2000).

[29] Z. Barticevic, M. Pacheco, C. A. Duque, and L. E. Oliveira, J. Phys. Condens. Matter **14**, 1021 (2002).

[30] X. Mi, D. Li, F. Meng, and H. Zhao, Chin. Opt. Lett. **7**, 335 (2009).

[31] M. Kira and S. W. Koch, Prog. Quantum Electron. **30**, 155 (2006).

[32] C. N. Böttge, B. Breddermann, L. Schneebeli, M. Kira, S. W. Koch, J. Bhattacharyya, H. Schneider, and M. Helm, Phys. Status Solidi C **10**, 1218 (2013).